Validation of Linear Covariance Techniques for Mars Entry, Descent, and Landing Guidance and Navigation Performance Analysis

James W. Williams*, William E. Brandenburg†
University of Illinois at Urbana-Champaign, Urbana, Illinois, 61801, USA

David C. Woffinden‡
NASA Johnson Space Center, Houston, Texas, 77058, USA

Zachary R Putnam§
University of Illinois at Urbana-Champaign, Urbana, Illinois, 61801, USA

Current Monte Carlo-based uncertainty analysis methods may require significant computational resources to evaluate the performance of a closed-loop guidance, navigation, and control system. An attractive alternative, particularly during the preliminary and conceptual design phase, is to use linear covariance analysis, which can provide the same statistical information as Monte Carlo methods at a fraction of the computational load. Linear covariance has already been demonstrated in various spaceflight regimes, but only recently has it been applied to atmospheric flight. In this study, a 6-degree-of-freedom formulation of both a linear covariance and Monte Carlo analysis tools are utilized for a Mars entry, descent, and landing scenario which capture both atmospheric and powered flight phases to support precision landing. Comparison of the performance results shows close agreement between the linear covariance and traditional Monte Carlo methods when incorporating an assortment of guidance algorithms and processing a variety of inertial and relative sensor measurements onboard the lander's navigation filter.

I. Introduction

The continued advancement of exploration missions to Mars and other selected celestial bodies place a greater emphasis on the ability to land mission-critical assets safely and precisely. The Safe and Precise Landing and Integrated Capabilities Evolution (SPLICE)[1] project focuses on refining and advancing precision landing and hazard avoidance technology. Particular emphasis is placed on the generation of navigation and sensor requirements for future entry, descent, and landing (EDL) systems.

A critical element of this safe and precise landing investment is gaining an understanding of the effects that uncertainties in mission design will have on the flight performance of candidate vehicles. The current standard for uncertainty analysis for EDL missions is Monte Carlo (MC) simulation techniques, which may require significant computational resources. Recently, linear covariance analysis (LinCov) techniques have been developed and demonstrated for atmospheric flight to enable rapid closed-loop, guidance, navigation, and control (GNC) performance analysis[2–4]. This paper serves to validate these new advances in EDL LinCov by comparing their outputs to those of an MC analysis.

While the extension of LinCov theories to include EDL scenarios is relatively new, there have been a number of studies already performed in this area. Initial entry-relevant LinCov studies include the one completed by Markley [5], which focused on IMU-based navigation during the entry pass of a vehicle using bank-angle steering. No trajectory dispersions were considered in Markley's study. More recently, Luo examined a "linear covariance-based model predictive control method for robust entry guidance design," which makes use of LinCov to perform optimal entry guidance[6]. Jin [2] also examined a closed-loop guidance and navigation assessment of an entry problem. Importantly, both Luo's and Jin's studies focused on three-degree-of-freedom (3-DOF) dynamics, which do not include vehicle attitude effects in their examinations.

*Graduate Research Assistant & NASA JSC Intern, Aerospace Engineering, AIAA Student Member
†Undergraduate Research Assistant & NASA JSC Intern, Aerospace Engineering, AIAA Student Member
‡GN&C Autonomous Flight Systems Branch, Aeroscience and Flight Mechanics Division, AIAA Professional Member
§Assistant Professor, Aerospace Engineering, AIAA Senior Member

The current study is the first to make use of a 6-DOF simulation framework for EDL LinCov that incorporates both inertial and relative sensor measurements in an onboard navigation filter, utilizes multiple guidance algorithms for both atmospheric and powered flight segments, and implements specific control algorithms that orient the spacecraft to evaluate the performance of an integrated closed-loop GN&C system. Since the system performance is intrinsically tied to it's attitude, the ability to perform 6-DOF analysis of an EDL scenario is considered of critical importance, particularly when gyros and accelerometers are core sensors used by the onboard navigation system and the entry guidance algorithm modulates the vehicle's lift by flying a specified angle of attack and varying the bank angle. It is also understood that this study is the first to incorporate a full EDL trajectory from entry interface (EI) to touchdown using propulsive descent and landing using linear covariance analysis techniques that is validated with Monte Carlo results.

The paper is organized as follows where Section II outlines the strategy assumed for the GN&C performance analysis, summarizes the Mars EDL trajectory and concept of operations, and defines the modeling assumptions. Section III provides the closed-loop GN&C performance results from both the EDL LinCov and Monte Carlo tools and highlights key metrics from the comparison, and Section IV makes final concluding observations.

II. GN&C Performance Analysis Overview and Modeling

This section provides an overview of the analysis techniques and performance metrics used to evaluate a Mars entry, descent, and landing scenario. It also outlines the specific EDL trajectory profile and concept of operations assumed for this study along with the models associated with the environment, vehicle, sensors, and guidance algorithms.

A. Generating GN&C Performance Metrics with LinCov and Monte Carlo Analysis

To analyze a GN&C system, whether using Monte Carlo or linear covariance analysis techniques, there are several key variables of interest that are utilized to characterize the system's integrated performance. As depicted in Figure 1, these variables include the environment dispersions $\delta\mathbf{x}$, the navigation dispersions $\delta\hat{\mathbf{x}}$, the actual navigation error $\delta\mathbf{e}$, and the onboard navigation error $\delta\hat{\mathbf{e}}$.

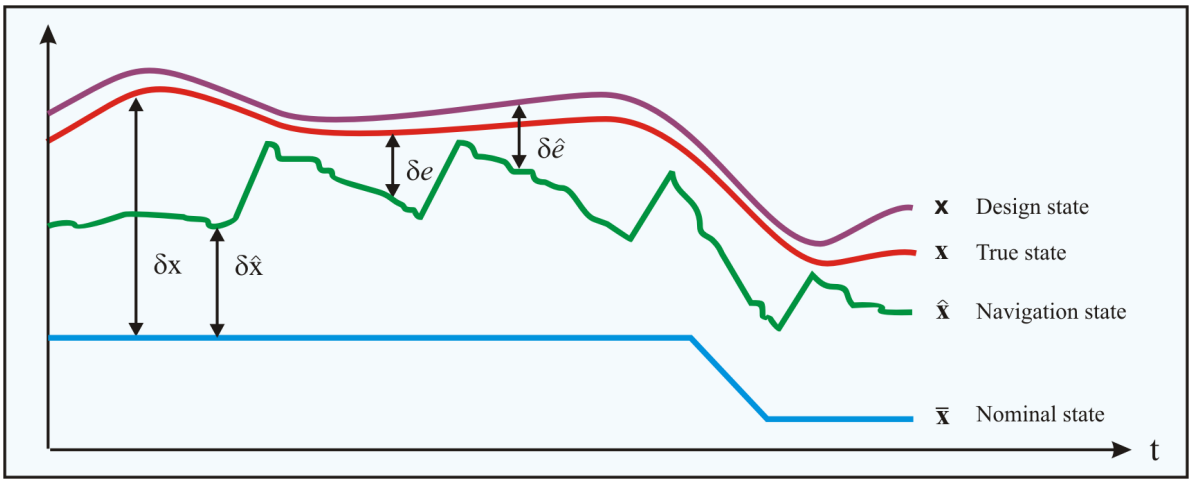

Fig. 1 GN&C performance metric variables.

The true dispersions $\delta\mathbf{x}$ are defined as the difference between the true state $\mathbf{x}$ and the nominal state $\bar{\mathbf{x}}$. The true state $\mathbf{x}$ is an n-dimensional vector that represents the *real world* environment or actual state.

$$\delta\mathbf{x} \stackrel{\Delta}{=} \mathbf{x} - \bar{\mathbf{x}} \qquad \mathbf{D} = E\left[\delta\mathbf{x}\delta\mathbf{x}^{\mathrm{T}}\right] \tag{1}$$

The nominal state $\bar{\mathbf{x}}$ is also an n-dimensional vector that represents the desired or reference state. The covariance of the environment dispersions, $\mathbf{D}$, indicates how precisely the system can follow a desired trajectory.

The navigation dispersions $\delta\hat{\mathbf{x}}$ are defined as the difference between the navigation state $\hat{\mathbf{x}}$ and the nominal state $\bar{\mathbf{x}}$.

The navigation state is an $\hat{n}$-dimensional vector ($\hat{n} < n$) that represents the filter's estimated state.

$$\delta\hat{\mathbf{x}} \triangleq \hat{\mathbf{x}} - \hat{\mathbf{N}}_x\bar{\mathbf{x}} \qquad\qquad \hat{\mathbf{D}} = E\left[\delta\hat{\mathbf{x}}\delta\hat{\mathbf{x}}^{\mathrm{T}}\right] \tag{2}$$

The matrix $\hat{\mathbf{N}}_x$ is an $(\hat{n} \times n)$ matrix that maps the estimated state in terms of the true and nominal state. The covariance of the navigation dispersions, $\hat{\mathbf{D}}$, reflect how precisely the onboard system thinks it can follow a prescribed reference trajectory.

The true navigation error $\delta\mathbf{e}$ is the difference between the environment and navigation states. It is also the difference between the environment and the navigation dispersions.

$$\delta\mathbf{e} \triangleq \hat{\mathbf{N}}_x\mathbf{x} - \hat{\mathbf{x}} = \hat{\mathbf{N}}_x\delta\mathbf{x} - \delta\hat{\mathbf{x}} \qquad\qquad \mathbf{P} = E\left[\delta\mathbf{e}\delta\mathbf{e}^{\mathrm{T}}\right] \tag{3}$$

The covariance of the true navigation error, $\mathbf{P}$, quantifies how precisely the onboard navigation system can estimate the actual state.

The onboard navigation error $\delta\hat{\mathbf{e}}$ itself is never computed, but it is used to develop the onboard navigation filter equations. It is defined as the difference between the design state, x, and the navigation state $\hat{\mathbf{x}}$.

$$\delta\hat{\mathbf{e}} \triangleq \mathrm{x} - \hat{\mathbf{x}} \qquad\qquad \hat{\mathbf{P}} = E\left[\delta\hat{\mathbf{e}}\delta\hat{\mathbf{e}}^{\mathrm{T}}\right] \tag{4}$$

The covariance of the onboard navigation error, $\hat{\mathbf{P}}$, quantifies how precisely the onboard navigation system expects it can determine the actual state. The performance of the onboard navigation system is determined by comparing $\hat{\mathbf{P}}$ to the actual navigation performance $\mathbf{P}$. If the *true* states and the *design* states are assumed to be the same, then the true navigation covariance will equal the onboard navigation covariance.

The covariances of the true dispersions, navigation dispersions, true navigation error, and the onboard navigation error are ultimately used to analyze and assess the performance of a proposed GN&C system. As illustrated in Figure 2, a common approach to obtain these performance metrics is to use a Monte Carlo simulation, where the sample statistics of hundreds or thousands of runs, N, are used to numerically compute the desired covariance matrices.

$$\mathbf{D} = \frac{1}{N-1}\sum \delta\mathbf{x}\delta\mathbf{x}^{\mathrm{T}} \qquad \hat{\mathbf{D}} = \frac{1}{N-1}\sum \delta\hat{\mathbf{x}}\delta\hat{\mathbf{x}}^{\mathrm{T}} \qquad \mathbf{P} = \frac{1}{N-1}\sum \delta\mathbf{e}\delta\mathbf{e}^{\mathrm{T}} \tag{5}$$

The onboard navigation error covariance $\hat{\mathbf{P}}$ is the navigation filter covariance for each run.

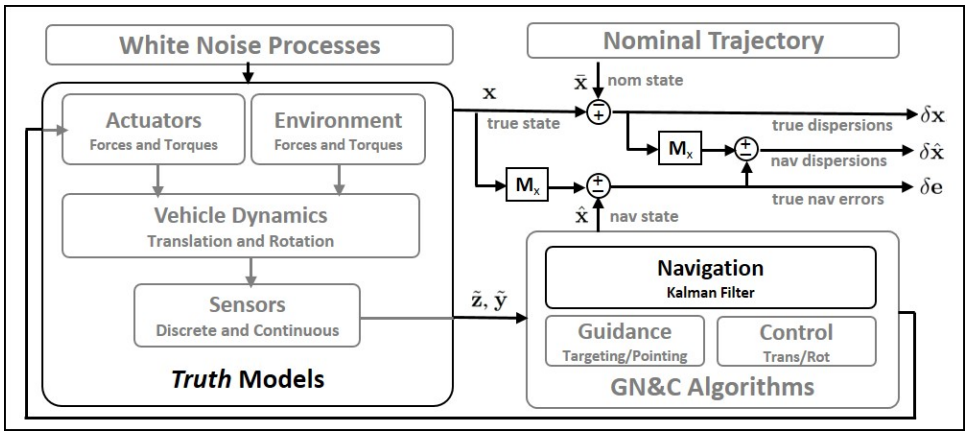

Fig. 2 GN&C performance metrics in a generic Monte Carlo simulation.

This same statistical information can be obtained using linear covariance analysis techniques. Linear covariance analysis incorporates the non-linear system dynamics models and GN&C algorithms to generate a nominal reference trajectory $\bar{\mathbf{x}}$ which is then used to propagate, update, and correct the onboard navigation covariance matrix $\hat{\mathbf{P}}$ and an augmented state covariance matrix $\mathbf{C}$,

$$\mathbf{C} = E\left[\delta\mathbf{X}\delta\mathbf{X}^{\mathrm{T}}\right] \tag{6}$$

where the augmented state $\delta\mathbf{X}^{\mathrm{T}} = [\delta\mathbf{x}^{\mathrm{T}}\ \delta\hat{\mathbf{x}}^{\mathrm{T}}]$ consists of the true dispersions and the navigation dispersions. Pre- and post-multiplying the augmented state covariance matrix by the following mapping matrices, the covariances for the trajectory dispersions, navigation dispersions, and the navigation error can be obtained.

$$\begin{aligned} \mathbf{D} &= [\,\mathbf{I}_{n\times n},\,\mathbf{0}_{n\times\hat{n}}\,]\,\mathbf{C}\,[\,\mathbf{I}_{n\times n},\,\mathbf{0}_{n\times\hat{n}}\,]^{\mathrm{T}} \\ \hat{\mathbf{D}} &= [\,\mathbf{0}_{\hat{n}\times n},\,\mathbf{I}_{\hat{n}\times\hat{n}}\,]\,\mathbf{C}\,[\,\mathbf{0}_{\hat{n}\times n},\,\mathbf{I}_{\hat{n}\times\hat{n}}\,]^{\mathrm{T}} \\ \mathbf{P} &= [\,\mathbf{I}_{\hat{n}\times n},\,-\mathbf{I}_{\hat{n}\times\hat{n}}\,]\,\mathbf{C}\,[\,\mathbf{I}_{\hat{n}\times n},\,-\mathbf{I}_{\hat{n}\times\hat{n}}\,]^{\mathrm{T}} \end{aligned} \tag{7}$$

Both the Monte Carlo and the linear covariance analysis techniques provide a complementary package that can generate the requisite statistical information using different approaches. The true dispersion covariance **D** and navigation covariance **P** derived in Eqn 5 and Eqn 7 can be compared to confirm expected performance results. Details regarding the fundamental linear covariance framework and equations used to govern the system dynamic models for both the LinCov and Monte Carlo simulation tools for atmospheric entry, descent, and landing were derived previously[3, 4].

B. Mars Entry, Descent, and Landing Scenario Overview

The scenario in this study is a facsimile of the Mars Science Laboratory (MSL) landing at Gale Crater, with the important distinction that it does not use a parachute for the descent segment, instead relying entirely on propulsive deceleration during the descent and landing segments of flight. This architecture is likely more representative of future EDL systems designed to deliver payloads greater than one ton to the surface[7, 8]. Many of the state parameters used in this study were acquired from Dutta [9].

As depicted in Figure 3, the simulation begins at entry interface (EI) and terminates at the targeted MSL's landing site summarized in Table 1. The vehicle's trajectory is split into three distinct phases of flight: entry, descent, and landing with the trajectory profile illustrated in Figure 4(a). During the entry phase, the Apollo Final Phase entry guidance algorithm is used to control range through bank-angle steering with the commanded and actual bank profile shown in Figure 4(b). The nominal crossrange with respect to the lander's velocity magnitude during the entry flight segment is highlighted in Figure 4(c). The crossrange deadband, plotted in black, scales with the square of the vehicle's velocity, and signifies where the vehicle must make a bank reversal.

During the atmospheric entry flight phase, the only sensor measurements available to the vehicle are the inertial measurement units (IMU), which are comprised of 3-axis accelerometers and gyroscopes. The termination of the

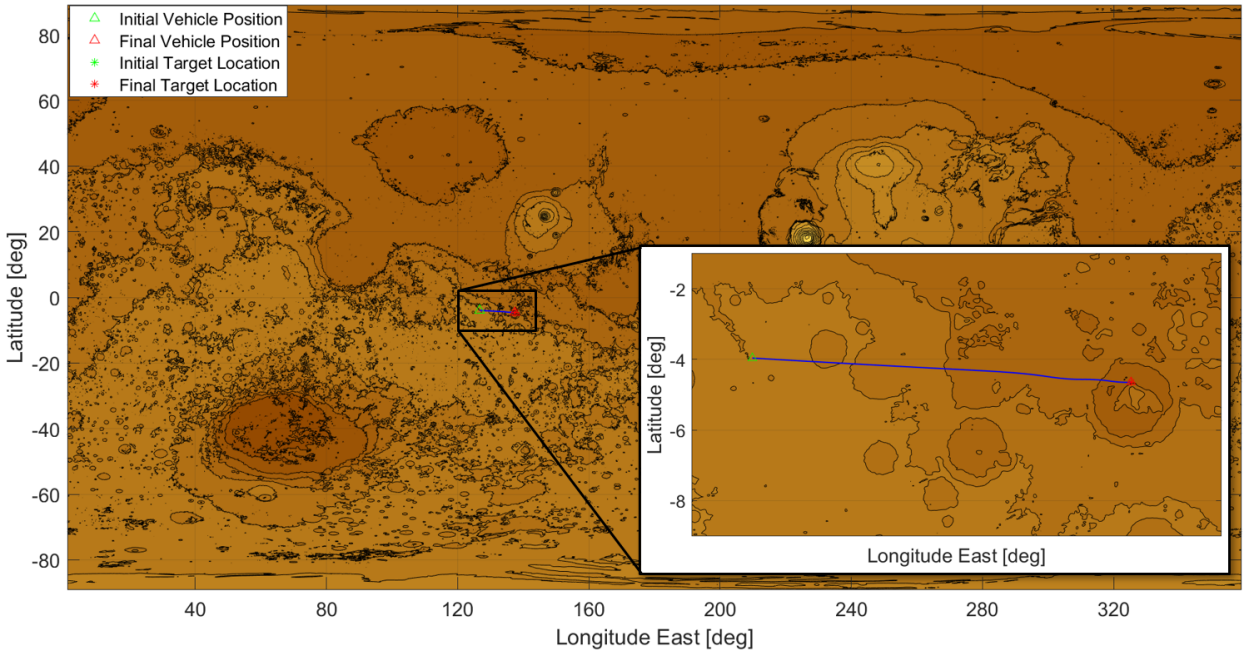

Fig. 3 Simulated Mars EDL Ground Track to Gale Crater.

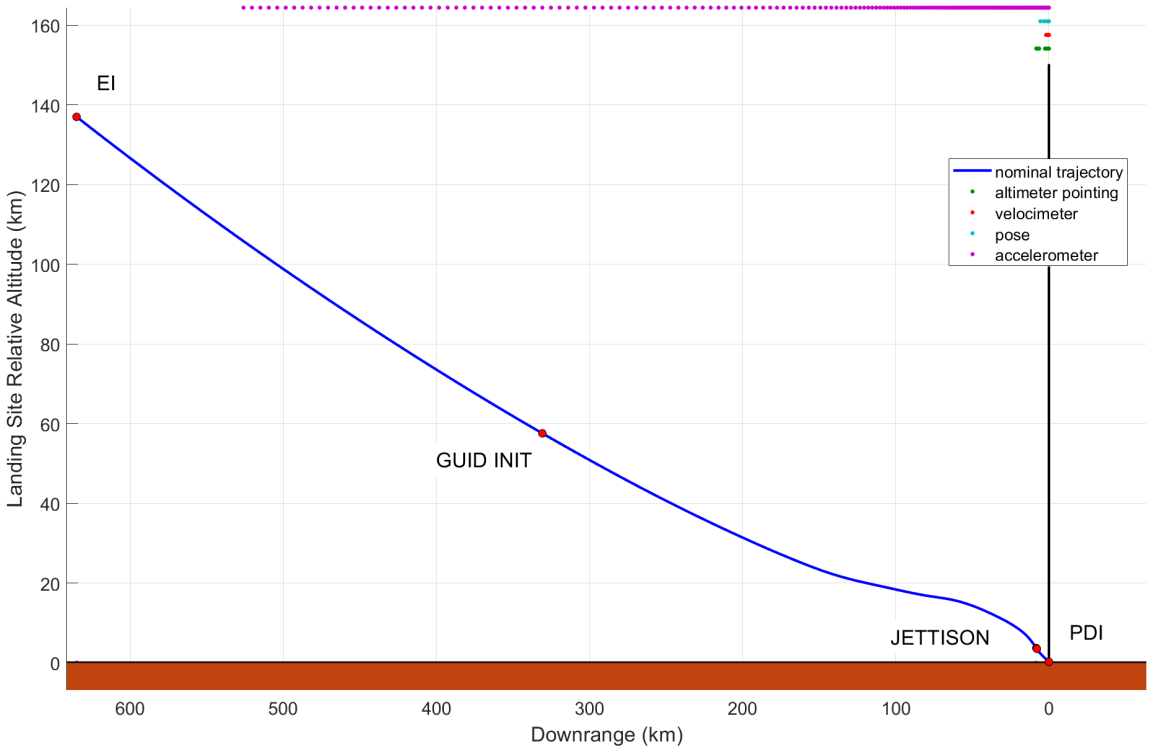

(a) Simulated Mars EDL Altitude Versus Downrange Trajectory Profile.

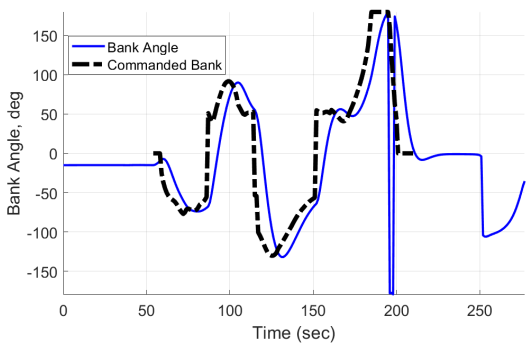

(b) Bank Angle Profile

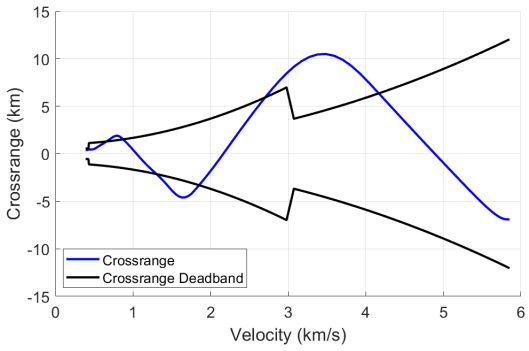

(c) Crossrange Versus Velocity

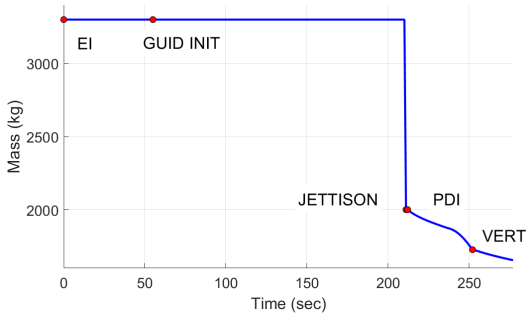

(d) Mass Profile

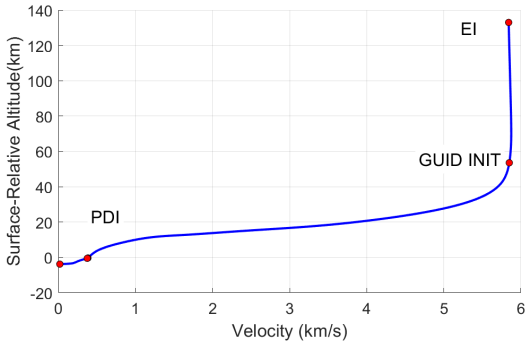

(e) Altitude Versus Velocity Profile

Fig. 4 Simulated Mars Nominal Entry Performance Parameters

entry phase is marked by a significant drop in the vehicle's mass, denoting the ejection of the forebody heatshield and backshell shwon in Figure 4(d) and subsequent exposure of thrusters and relative sensors to the environment. The relative sensors used in this study are a doplidar altimeter/velocimeter and a pose terrain-relative navigation (TRN) sensor. At this time, the vehicle switches to a linear acceleration fixed time-to-go propulsive descent algorithm[10] to deliver the vehicle to a point directly above the landing site with zero horizontal velocity at a target-relative altitude of 200 m and descent rate of 20 m/s. Once the vehicle has reached this point above the landing site, it transitions to a propulsive vertical descent algorithm that linearly decrease the descent rate as a function of altitude such that at touch down the vehicle vertical velocity is 1 m/s. The velocity profile versus altitude is provided in Figure 4(e). The simulation concludes at touchdown. More detail on the guidance algorithms used is available in [4].

Table 1 Initial Lander and Landing Site States

MSL Entry Interface State	**Value**
Altitude, km	133 [9]
Azimuth (inertial), deg	93.2065 [9]
Flight-Path Angle (inertial), deg	-15.489 [9]
Latitude, deg	-3.9186 [9]
Longitude, deg	126.72 [9]
Angle of Attack, deg	-10
Angle of Bank, deg	-15

Gale Crater Landing Site	**Value**
Altitude, km	-4 [9]
Latitude, deg	-4.5895 [9]
Longitude, deg	137.4417 [9]

C. Modeling

1. Environment Model

Mars is modeled as a rotating spheroid with an inverse-square gravity field modified by J2 effects. The landing site is located at -4.0 km altitude relative to the spheroid. The atmosphere model used is the Mars Global Reference Atmospheric Model (GRAM) 2010, based on conditions anticipated during the flight profile of MSL. A lookup table was created from 1000 individual samples of Mars GRAM from an altitude of -4.5 km to 150 km. The model consists of nominal and standard deviation values for density and u, v, and w winds as functions of altitude. The nominal values are averaged from the samples, while standard deviations are calculated from the individual samples. Summary of the Mars environment model parameters are provided in Table 2.

Table 2 Simulated Mars Environment Parameters

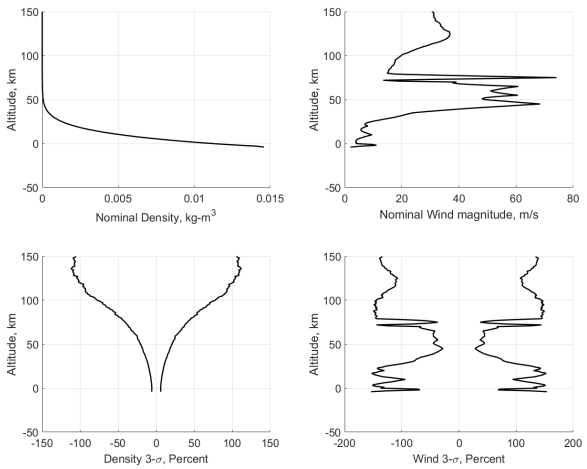

Parameter	**Value**
Surface Model	Spheroid
Equatorial Radius, km	3396
Flattening Ratio, nd	0.00589
Rotation Rate, rad/s	7.09×10^{-5}
Atmosphere Model	Mars GRAM
Gravitational Parameter, m^3/s^2	4.289×10^{13}
J2 Perturbation, nd	1.96×10^{-3}

2. Vehicle Model

The vehicle is modeled as MSL, as summarized in Table 3. The vehicle begins flight at a mass of 3300 kg with a 70-deg sphere-cone aerodynamic model and a reference area of 15.9 m^2, and flies at a nominal angle of attack of -10 degrees measured from the heatshield. At the end of entry guidance, the aeroshell is jettisoned, corresponding to a 1300 kg loss of mass to the vehicle. Eight thrusters are then ignited, with maximum thrust magnitudes of 3600 N each. The thrusters are modeled as one overall force on the vehicle, with an aggregate specific impulse (I_{SP}) of 267 s. The thruster uncertainty parameters are shown in Table 4. The uncertainty parameters in the simulation are comprised of initial uncertainties and process noises, as shown in Table 5.

Table 3 MSL vehicle modeling parameters

Parameter	Value
Initial Mass, kg	3300
Aeroshell Drop Mass, kg	1300
Aerodynamics	MSL-like spherecone
Reference Area, m^2	15.9
Thruster ISP, s	267
Thruster number	8
Thruster Max Thrust, N	3600 (Each)

Table 4 Thruster dispersions.

Parameter	3-σ value
Bias, N	250
Scale Factor, nd	1×10^{-3}
Misalignment, deg	0.02
ISP Bias, s	10

Table 5 Lander dispersion sources and values.

Parameter	3-σ value
Initial Position, km	[1.0,1.0,1.0]
Initial Velocity, m/s	[1.0,1.0,1.0]
Initial Attitude, deg	[0.3,0.2,0.25]
Initial Attitude Rate, deg/s	[0.01,0.01,0.01]
Initial Navigation Position Error, m	[21.1,53.1,19.4]
Initial Navigation Velocity Error, m/s	[0.0275, 0.0234, 0.0258]
Initial Navigation Attitude Error, deg	1×10^{-4}
Initial Navigation Attitude Rate Error, deg/s	7×10^{-7}
Translational Process Noise, m/s/$\sqrt{s}$	1.2×10^{-3}
Rotational Process Noise, rad/s/$\sqrt{s}$	1×10^{-6}

3. Sensor Models

Accelerometer The accelerometer measures the non-gravitational acceleration in the IMU case frame $\tilde{\mathbf{a}}^{imu}$, which is a function of the nominal inertial-to-body transformation matrix $\bar{\mathbf{T}}_i^b$, the nominal body-to-IMU transformation $\bar{\mathbf{T}}_b^{imu}$, the actual attitude dispersion $\boldsymbol{\theta}$, the misalignment $\boldsymbol{\mu}_a$, the constant scale factor $\mathbf{s}_a$, the Markov scale factor $\boldsymbol{\sigma}_a$, the constant bias $\mathbf{b}_a$, the Markov bias $\boldsymbol{\beta}_a$, the nonorthogonality factor $\boldsymbol{\gamma}_a$, and the velocity random walk (noise) $\boldsymbol{\upsilon}_a$.

$$\tilde{\mathbf{a}}^{imu} = (\mathbf{I} + [(\mathbf{s}_a + \boldsymbol{\sigma}_a)\diagdown]) \left[(\mathbf{I} + [\boldsymbol{\mu}_a \times]) \, (\mathbf{I} + [\boldsymbol{\gamma}_a *]) \, \bar{\mathbf{T}}_b^{imu} \, (\mathbf{I} + [\boldsymbol{\theta} \times]) \, \bar{\mathbf{T}}_i^b \mathbf{a}^i + \mathbf{b}_a + \boldsymbol{\beta}_a + \boldsymbol{\upsilon}_a \right] \tag{8}$$

The navigation filter processes a compensated accelerometer measurement $\hat{\mathbf{a}}^i$ with the estimated accelerometer biases $\hat{\mathbf{b}}_a$ and $\hat{\boldsymbol{\beta}}_a$, misalignment $\hat{\boldsymbol{\mu}}_a$, non-orthogonality $\hat{\boldsymbol{\gamma}}_a$, scale factor terms $\hat{\mathbf{s}}_a$ and $\hat{\boldsymbol{\sigma}}_a$, and attitude state $\hat{\boldsymbol{\theta}}$. The compensated accelerometer measurement is given by

$$\hat{\mathbf{a}}^i = \bar{\mathbf{T}}_b^i \left(\mathbf{I} - [\hat{\boldsymbol{\theta}} \times] \right) \bar{\mathbf{T}}_{imu}^b \, (\mathbf{I} - [\hat{\boldsymbol{\gamma}}_a *]) \, (\mathbf{I} - [\hat{\boldsymbol{\mu}}_a \times]) \left[(\mathbf{I} - [(\hat{\mathbf{s}}_a + \hat{\boldsymbol{\sigma}}_a)\diagdown]) \, \tilde{\mathbf{a}}^{imu} - \hat{\mathbf{b}}_a - \hat{\boldsymbol{\beta}}_a \right] \tag{9}$$

The uncertainty parameters used for the accelerometer are listed in Table 6.

Gyro The gyros measure the vehicle's angular rates in the IMU case frame $\tilde{\boldsymbol{\omega}}^{imu}$ and is represented as a function of the nominal body-to-IMU transformation $\bar{\mathbf{T}}_b^{imu}$ where b indicates the vehicle body-fixed frame, the misalignment $\boldsymbol{\mu}_\omega$, the constant scale factor $\mathbf{s}_\omega$, the Markov scale factor $\boldsymbol{\sigma}_\omega$, the constant bias $\mathbf{b}_\omega$, the Markov bias $\boldsymbol{\beta}_\omega$, the nonorthogonality factor $\boldsymbol{\gamma}_\omega$, and the angular random walk (noise) $\boldsymbol{\upsilon}_\omega$

$$\tilde{\boldsymbol{\omega}}^{imu} = (\mathbf{I} + [(\mathbf{s}_\omega + \boldsymbol{\sigma}_\omega)\diagdown]) \left[(\mathbf{I} + [\boldsymbol{\mu}_\omega\times]) \, (\mathbf{I} + [\boldsymbol{\gamma}_\omega *]) \, \bar{\mathbf{T}}_b^{imu} \boldsymbol{\omega}^b + \mathbf{b}_\omega + \boldsymbol{\beta}_\omega + \boldsymbol{\upsilon}_\omega \right] \tag{10}$$

The compensated gyro measurement $\hat{\boldsymbol{\omega}}^b$ utilized by the navigation filter incorporates the estimated biases $\hat{\mathbf{b}}_\omega$ and $\hat{\boldsymbol{\beta}}_\omega$, scale factors $\hat{\mathbf{s}}_\omega$ and $\hat{\boldsymbol{\sigma}}_\omega$, misalignment $\hat{\boldsymbol{\mu}}_\omega$, and non-orthogonality $\hat{\boldsymbol{\gamma}}_\omega$ states

$$\hat{\boldsymbol{\omega}}^b = \bar{\mathbf{T}}_{imu}^b \, (\mathbf{I} - [\hat{\boldsymbol{\gamma}}_\omega *]) \, (\mathbf{I} - [\hat{\boldsymbol{\mu}}_\omega\times]) \left[(\mathbf{I} - [(\hat{\mathbf{s}}_\omega + \hat{\boldsymbol{\sigma}}_\omega)\diagdown]) \, \tilde{\boldsymbol{\omega}}^{imu} - \hat{\mathbf{b}}_\omega - \hat{\boldsymbol{\beta}}_\omega \right] \tag{11}$$

The uncertainty parameters used for the gyroscope are listed in Table 7.

NDL Altimeter The NASA doplidar (NDL) altimeter has three beams separated by a specified angular distance where each beam provides a range measurement to the planet surface[12, 13]. The instrument is fixed in the body frame and measures the relative distance to the surface $\tilde{\rho}_{alt}$. The measurement is a function of the true surface range ρ, the scale factor s_{alt}, a bias b_{vel}, a Markov bias capturing the variations in the topography b_{ter}, and sensor noise ν_{alt}.

$$\tilde{\rho}_{alt} = \rho \, (1 + s_{alt}) + b_{alt} + b_{ter} + \nu_{alt} \tag{12}$$

The true range between each beam's boresight and the surface can be expressed as a function of the vehicle's inertial-to-body transformation $\mathbf{T}_i^b$, the line-of-sight direction of the beam $\mathbf{u}_{beam}^b$, and the inertial position of the sensor mounted on the vehicle, $\mathbf{r}_{alt}^i$. This can be obtained by utilizing the following equality that relates the radius of the planet surface at the point of altimeter signal contact R_s with the vehicle's inertial position vector $\mathbf{r}^i$

$$R_s^2 = |\mathbf{r}_{alt}^i + \mathbf{T}_b^i \, \mathbf{u}_{beam}^b \rho|^2 \tag{13}$$

Expanding the above equation, gives

$$\rho^2 + 2\rho \left(\mathbf{T}_b^i \, \boldsymbol{i}_{alt}^b \right)^{\mathrm{T}} \mathbf{r}_{alt}^i + |\mathbf{r}_{alt}^i|^2 - R_s^2 = 0 \tag{14}$$

This quadratic polynomial in ρ can be used to solve for the true altimeter distance, ρ. The uncertainty parameters used for the altimeter are listed in Table 8.

NDL Velocimeter The NASA doplidar (NDL) velocimeter utilizes three beams generally aligned in a tetrahedron orientation to measure the relative velocity between the instrument and the planet surface. For each beam, the line-of-sight velocity or relative range-rate measurement to the surface $\tilde{v}_{vel}$ can be expressed as a function of the beam direction in the body frame $\mathbf{u}_{beam}^b$, the inertial-to-body transformation matrix $\mathbf{T}_i^b$, the inertial velocity of the velocimeter sensor $\mathbf{v}_{vel}^i$, the inertial position of the instrument $\mathbf{r}_{vel}^i$, the planets angular rate $\boldsymbol{\omega}_p^i$, a bias b_v, and measurement noise ν_{vel}.

$$\tilde{v}_{vel} = \left(\mathbf{u}_{beam}^b \right)^T \mathbf{T}_i^b \left(\mathbf{v}_{vel}^i - \boldsymbol{\omega}_p^i \times \mathbf{r}_{vel}^i \right) + b_v + \nu_{vel} \tag{15}$$

The uncertainty parameters used for the velocimeter are listed in Table 9.

Terrain Relative Sensor The TRN system generates a six degree-of-freedom position and orientation measurement relative to the surface. The measurement is modeled with a constant and a Markov bias. The relative position vector in the TRN frame is given by the equation

$$\tilde{\mathbf{r}}_{rel}^{trn} = \mathbf{T}_b^{trn} \mathbf{T}_i^b (\mathbf{r}_t - \mathbf{r}_c) + \mathbf{b}_\rho^{trn} + \boldsymbol{\beta}_\rho^{trn} + \boldsymbol{\eta}_\rho^{trn} \ , \tag{16}$$

where $\mathbf{r}_t$ and $\mathbf{r}_c$ are the target and chaser inertial position vectors, $\mathbf{b}_\rho^{trn}$ is the relative position constant bias, $\boldsymbol{\beta}_\rho^{trn}$ is the relative position Markov bias, and $\boldsymbol{\eta}_\rho^{trn}$ is the relative position measurement noise.

The relative attitude measurement in the TRN sensor frame is processed as a derived measurement, $\tilde{\boldsymbol{\theta}}_{rel}^{trn}$. It is effectively the residual to be processed by the onboard navigation filter,

$$\boldsymbol{I} - \left[\tilde{\boldsymbol{\theta}}_{rel}^{trn} \times \right] = \tilde{\mathbf{T}}_t^{trn} \left[\hat{\mathbf{T}}_i^t \hat{\mathbf{T}}_c^i \hat{\mathbf{T}}_{trn}^c \right] \tag{17}$$

where the estimate of the derived relative attitude measurement is a function of the target attitude uncertainty $\boldsymbol{\theta}_t^t$, the chaser attitude error state $\boldsymbol{\theta}_c^c$, the constant bias $\mathbf{b}_\theta^f$, a Markov bias $\boldsymbol{\beta}_\theta^f$, and noise $\boldsymbol{\eta}_\theta^f$.

$$\tilde{\boldsymbol{\theta}}_{rel}^{trn} = \hat{\mathbf{T}}_t^{trn}\boldsymbol{\theta}_t^t - \hat{\mathbf{T}}_c^{trn}\boldsymbol{\theta}_c^c + \mathbf{b}_\theta^{trn} + \boldsymbol{\beta}_\theta^{trn} + \boldsymbol{\eta}_\theta^{trn} \tag{18}$$

The uncertainty parameters used for the TRN are listed in Table 10.

Table 6 Accelerometer Uncertainty Parameters

Parameter	3-sigma value
Velocity Random Walk, $\mu g/\sqrt{Hz}$	150
Bias, μg	100
Scale Factor, ppm	175
Nonorthogonality, arcsec	15
Markov Bias, μg	15
Markov Scale Factor, ppm	175

Table 7 Gyroscope Uncertainty Parameters

Parameter	3-sigma value
Angular Random Walk, deg/$\sqrt{hr}$	0.018
Bias, deg/hr	0.15
Scale Factor, ppm	15
Nonorthogonality, arcsec	75
Markov Bias, deg/hr	0.09
Markov Scale Factor, ppm	15

Table 8 NDL Altimeter Uncertainty Parameters

Parameter	3-sigma value
Noise, m	6.6
Bias, m	1.5
Scale factor, %	0.1
Misalignment, arcsec	150
Min/Max Altitude	20 m / 6 km
Measurement Frequency, Hz	1

Table 9 NDL Velocimeter Uncertainty Parameters

Parameter	3-sigma value
Noise, m/s	0.051
Bias, m/s	0.030
Scale Factor, %	0.25
Misalignment, arcsec	50
Max Vel/Altitude	200 m/s and 4 km
Measurement Frequency, Hz	1

Table 10 Terrain Relative Navigation Uncertainty Parameters

Parameter	3-sigma value
Position Noise, m	15
Attitude Noise, deg	1.5
Position Bias, m	3
Attitude Bias, deg	0.1
Measurement Frequency, Hz	0.1

III. Mars EDL GN&C Performance Result Comparisons

In this analysis, the nominal trajectory created by LinCov is being compared against a "nominal MC" trajectory, which is the trajectory calculated by the MC framework in the absence of dispersions. This is different than the "average MC" trajectory to which many uncertainty analyses compare dispersions. In this analysis, a 200-sample MC simulation was compared to a similar LinCov simulation to assess how closely LC is able to match the results from MC. For clarity of some of the plots, only some of the individual MC samples are being shown. The resultant dispersion information in the plots is being calculated from the full amount of MC samples.

Figure 5(a) shows the full trajectory in terms of altitude vs. downrange. The scenario begins with the vehicle roughly 650 km downrange from the target at a target-relative altitude of 137 km. The LinCov and MC nominal trajectories track each other nearly identically, reaching the target site at the same timestep. Figure 5(b) shows the

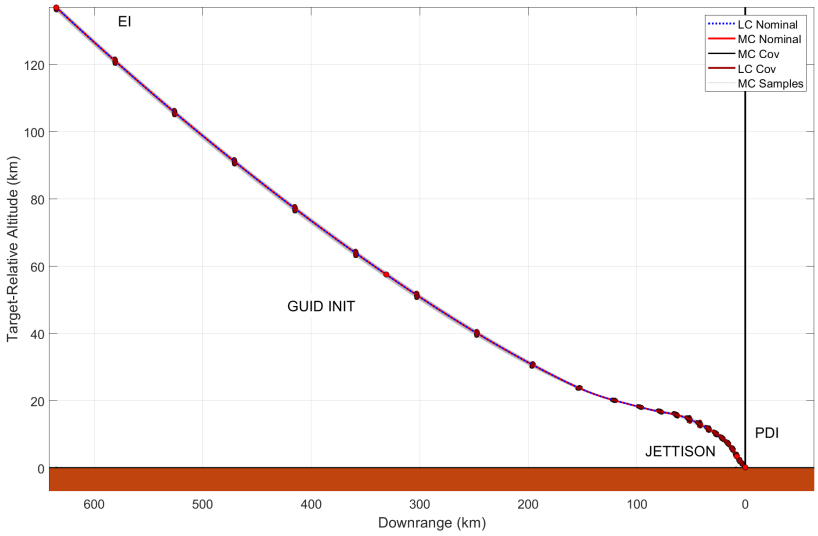

(a) Full trajectory

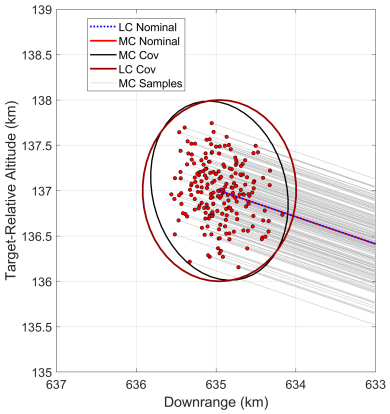

(b) Initial Uncertainty

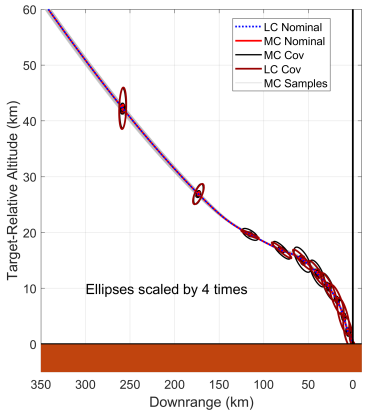

(c) Entry

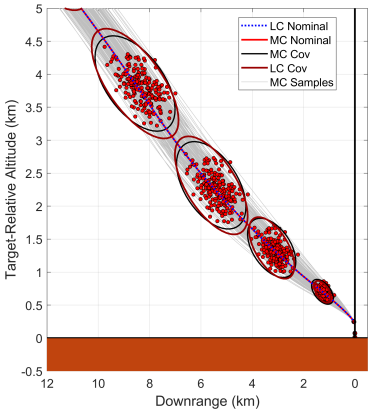

(d) Descent

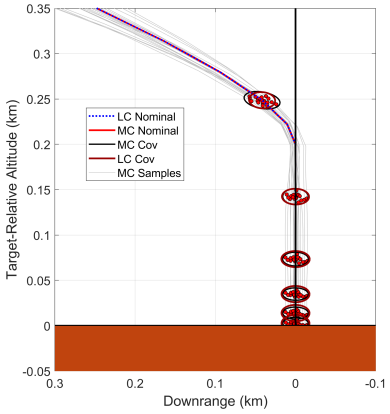

(e) Landing

Fig. 5 Altitude Versus Downrange Trajectory Dispersions

initial covariance ellipse for both the LinCov and MC frameworks. This figure demonstrates that the two frameworks are initializing the uncertain scenario in similar ways. Figures 5(c) to 5(e) show detail views of the entry, descent, and landing portions of the trajectory, respectively. Figure 5(c), with covariance ellipses scaled up for clarity, shows nearly identical covariance ellipses being predicted by both the LinCov and MC frameworks. Figure 5(d) shows that the two frameworks are predicting similar decreases in uncertainty as the vehicle comes under propulsive control and targets the vertical descent initiation site. Finally, 5(e) shows the landing portion of the trajectory, showing nearly identical covariance ellipses between the two frameworks as the vehicle lowers itself to touchdown.

Figure 6(a) shows the position dispersion ellipse in downrange vs. crossrange at touchdown, confirming that the two frameworks are predicting uncertainties in touchdown position which are quite close to each other. Figure 6(b) similarly shows the touchdown velocity dispersion ellipses at touchdown compare well between LinCov and MC.

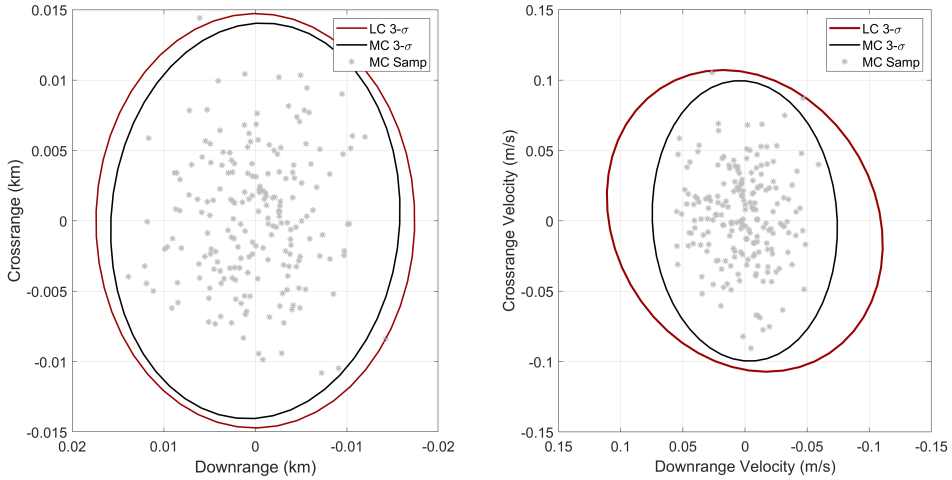

(a) Position Footprint

(b) Velocity Footprint

Fig. 6 Downrange Versus Crossrange Landing Footprint Dispersions

Figures 7(a) to 7(c) show the navigation performance as a function of time for the vehicle from EI to touchdown. In each case, the vehicle is using only its IMU until roughly 3.75 minutes. At this point, the front aeroshell is jettisoned and the altimeter, velocimeter, and TRN are able to activate, improving the navigation solution. Overall, the agreement between LinCov and MC is excellent in this area. Because MC simulation has many samples with their own navigation solutions, some individual samples take longer to drive down the navigation error, causing the overall navigation error to ramp down over time instead of decrease in the space of a timestep. This is an artifact of of MC simulation which cannot be replicated in an LinCov analysis.

Figure 8(a) shows the full trajectory in terms of altitude vs. velocity. Figure 8(b) shows that the initial dispersion ellipses are nearly identical between LinCov and MC. Figures 8(c) to 8(e) show the entry, descent, and landing segments of the trajectory, demonstrating sustained good agreement between LinCov and MC. Figure 8(d) shows the LC ellipses predicting slightly larger ellipses than the MC framework, but these differences are relatively small.

Figure 9(a) shows the trajectory in terms of downrange vs. crossrange. Figure 9(b) shows the initial dispersion ellipse, with good agreement between the two frameworks. Figure 9(c) shows the entry portion of the trajectory, showing a single outlier MC trajectory near the end of the entry segment, but otherwise good agreement between LinCov and MC. Figure 9(d) shows the first bank reversal maneuver of the trajectory. Before the reversal, there is very good agreement between LinCov and MC, but afterward the MC framework is estimating trajectories much more spread in crossrange than the LC framework. This is an effect of the bank reversal being an event based on state and not time. An underlying assumption of LinCov theory is that events do not vary in time with dispersions, but this is not the case for the bank reversal maneuver. Methods known as event triggers [14] can be used to improve the covariance of an LinCov trajectory subject to state-based events, but have not yet been applied to this particular event. It is believed that the inclusion of event triggers would bring LinCov and MC into much closer agreement in the area immediately post-bank reversal. Despite both the outlier trajectory and the disagreement caused by the bank reversal, Figure 9(e)

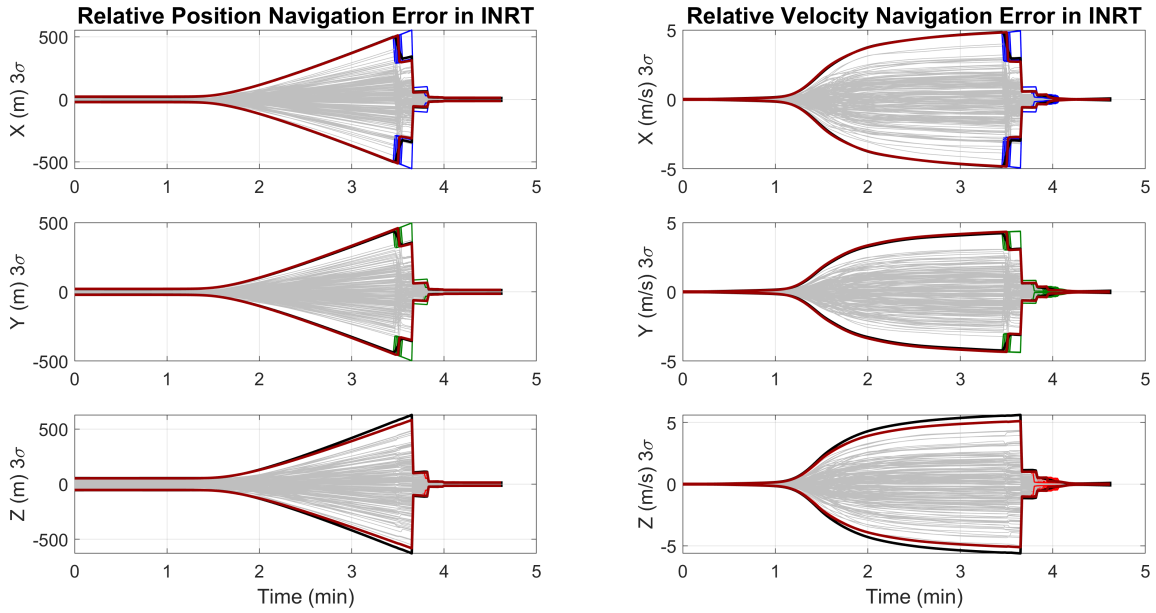

(a) Relative Position

(b) Relative Velocity

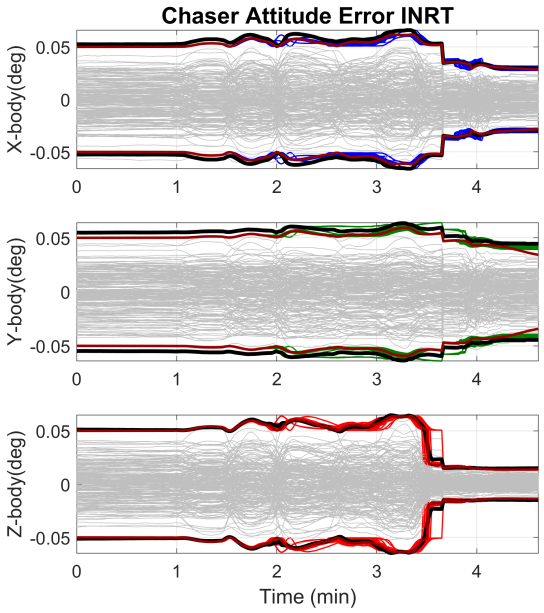

(c) Body Attitude

Fig. 7 Relative Navigation Errors Expressed in the Inertial Frame

shows good agreement between LinCov and MC in the trend of the trajectory to shrink dispersions down to the target landing site. Landing is not shown in this view, because the landing takes place nearly entirely vertically, so little detail is visible.

Figure 11(a) shows the dynamic pressure vs. time for the trajectory. There is good agreement throughout the trajectory, especially at the peak dynamic pressure shown in the inset. Figures 10(a) and 10(b) show the delta-V and mass dispersions for the vehicle, respectively. While there is some disagreement during the descent segment, the LinCov

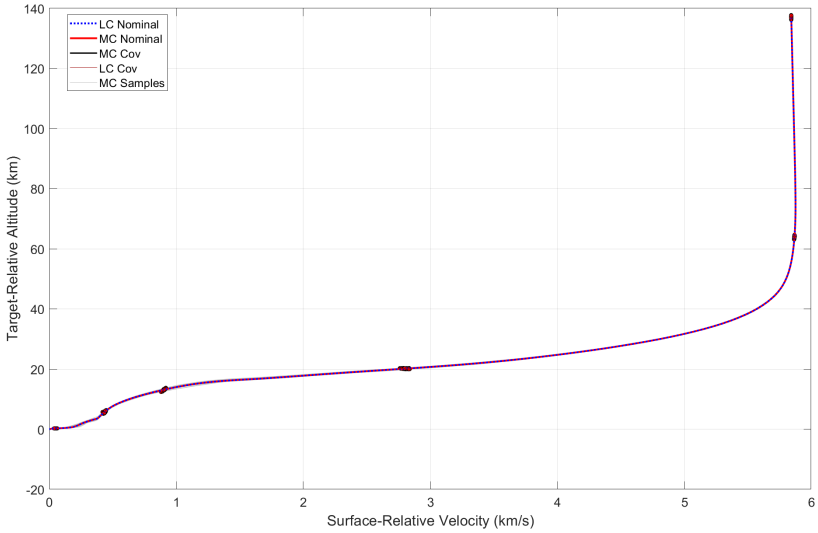

(a) Full trajectory

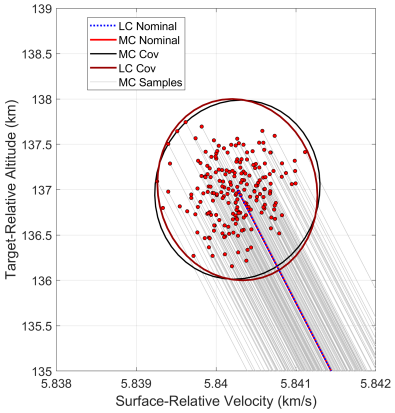

(b) Initial Uncertainty

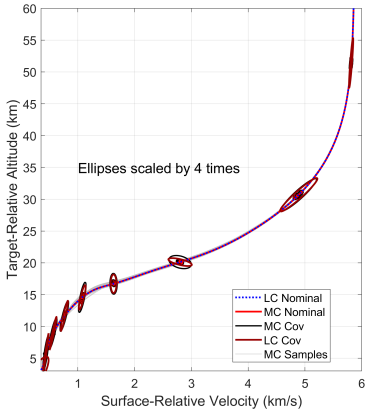

(c) Entry

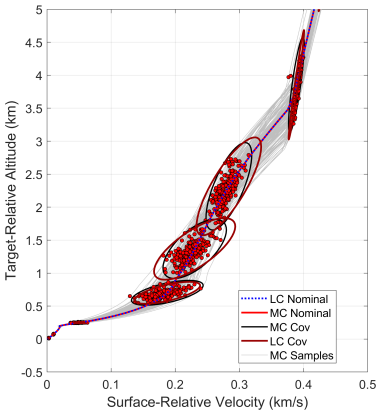

(d) Descent

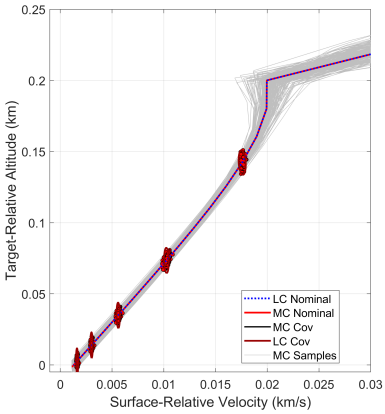

(e) Landing

Fig. 8 Velocity Versus Altitude Trajectory Dispersions

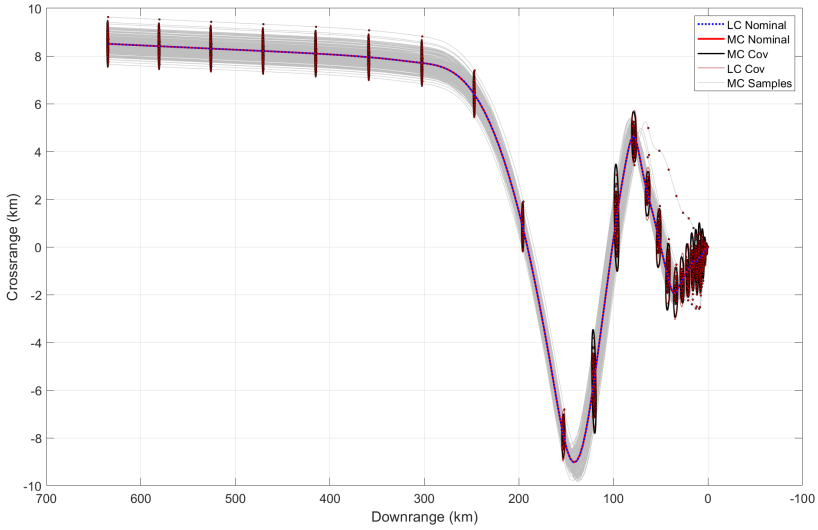

(a) Full trajectory

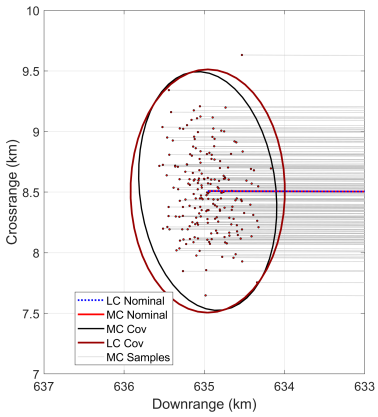

(b) Initial Uncertainty

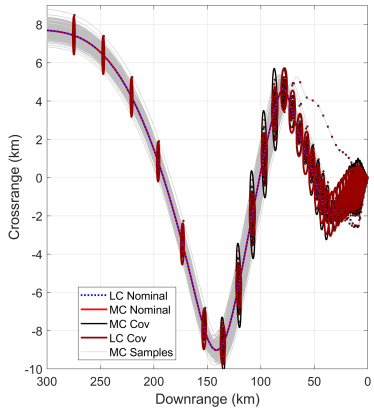

(c) Entry

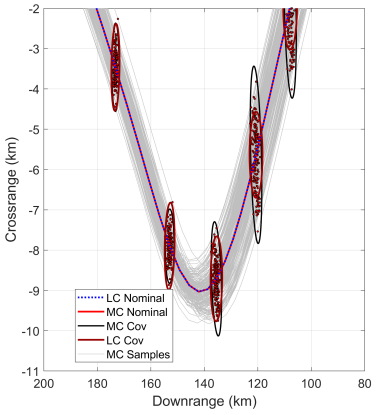

(d) Bank Reversal

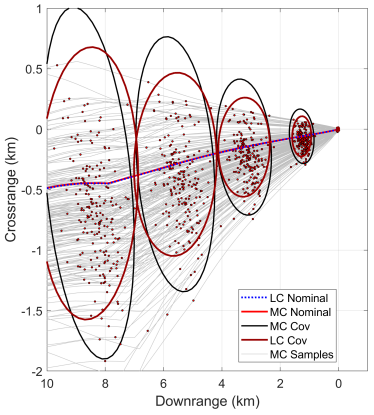

(e) Descent

Fig. 9 Crossrange Versus Downrange Trajectory Dispersions

and MC frameworks agree very closely during the vertical descent segment. Finally, Figure 11(b) shows the velocity vs. time for the propulsive descent segment of flight. Similarly to the delta-V and mass dispersion plots, the LC and MC frameworks show some disagreement during the descent segment of flight which is cleaned up at the vertical descent initiation time.

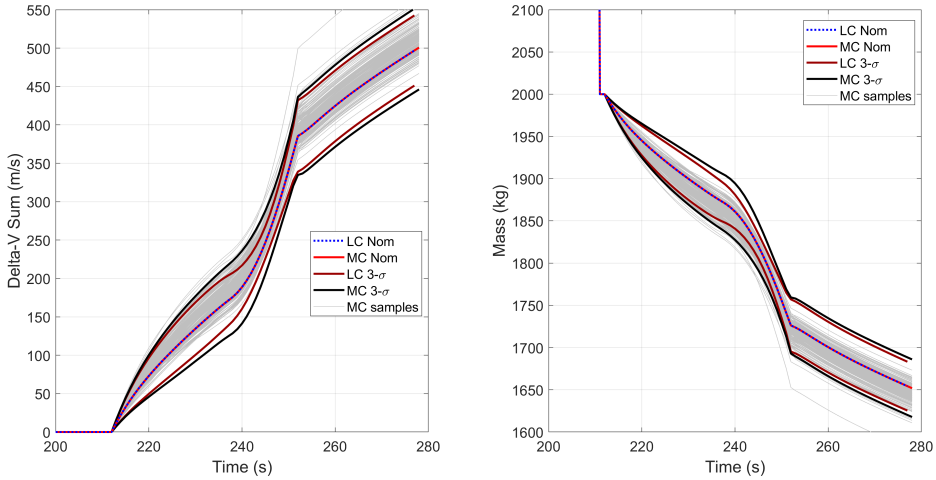

(a) Delta-v Dispersions (b) Mass (Propellant) Dispersions

Fig. 10 Propellant Dispersion Metrics

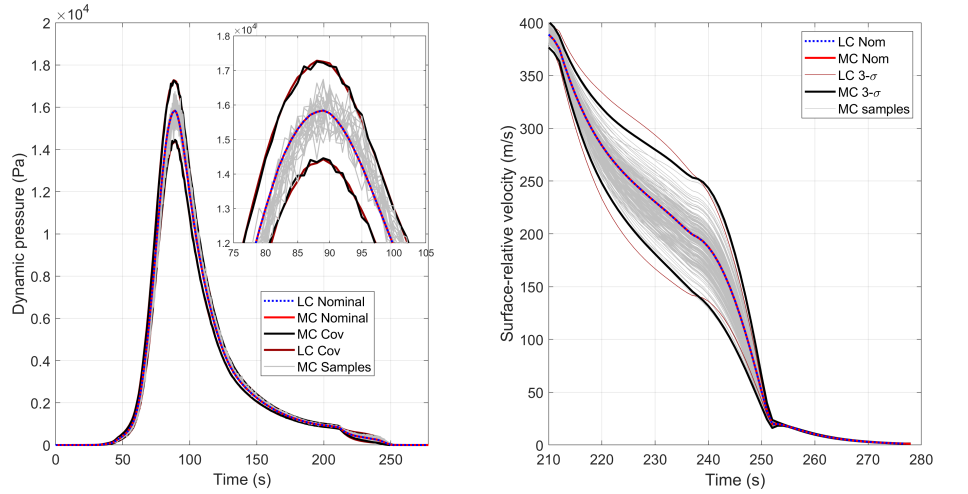

(a) Dynamic Pressure Dispersions (b) Velocity Dispersions during propulsive flight segment

Fig. 11 Aero Dispersions Metrics

More quantitative comparisons between some parameters are shown in Table 11. While variations do exist between the dispersions estimated by LinCov and MC, they are commonly within 10% of each other, which is a reasonable expectation for comparisons between LinCov and MC, and highlights the fact that LinCov should be used as a complement to MC and not a full replacement.

Table 11 Comparison of various nominal and dispersed values

Value	LC Nominal	LC 3-σ	MC Nominal	MC 3-σ	Nom + 3-σ Percent Diff
Max Delta-V, m/s	496.87	48.93	496.87	54.45	1.01
Final Mass, kg	1654.3	28.08	1654.3	33.9	0.35
Dynamic Pressure, Pa	15837	1412.7	15837	1381.8	0.18
Touchdown Downrange, m	0	52.2	0	47.4	9.64
Touchdown Crossrange, m	0	44.1	0	42	4.88

IV. Conclusion

This paper shows that good agreement between Monte Carlo and LinCov techniques for estimating the uncertainties in an end-to-end EDL mission at Mars. Uncertainties in parameters such as atmospheric properties, sensor readings, initial states, and vehicle properties were input in the two analysis frameworks and generated similar uncertainties in multiple aspects of the mission analysis, including the flight dynamics, sensor & navigation performance, landed accuracy, and delta-V usage. Additionally, the results showed good agreement in more traditional EDL-relevant plots, such as altitude vs. velocity and dynamic pressure vs. time. It is apparent that there are still some areas where improvement to the linear covariance formulation may be necessary to give better agreement between the two frameworks, most apparent of these being the discrepancies that arise during the bank-angle reversals during the entry phase overall takeaway, results from from this effort indicate that EDL LinCov is rapidly approaching a level of maturity that will enable it to complement MC analyses for early-mission design uncertainty studies for EDL missions, finally extending the capabilities of LinCov from launch trajectories, in-space trajectories, all the way to EDL trajectories, enabling rapid, end-to-end mission simulation for many systems of interest.

Acknowledgments

This work was primarily developed under the Safe and Precise Landing and Integrated Capabilities Evolution (SPLICE) project with additional support from the Graduate Assistance in Areas of National Need (GAANN) fellowship program and facilitated through the NASA Space Act Agreement between the NASA Johnson Space Center and the University of Illinois at Urbana-Champaign, SAA-EA-20-31386.

References

[1] Sostaric, R. R., Pedrotty, S., Carson, J. M., Estes, J. N., Amzajerdian, F., Dwyer-Cianciolo, A. M., and Blair, J. B., "The SPLICE Project: Safe and Precise Landing Technology Development and Testing," *AIAA Scitech 2021 Forum*, 2021. https://doi.org/10.2514/6.2021-0256.

[2] Jin, K., Geller, D., and Luo, J., "Development and Validation of Linear Covariance Analysis Tool for Atmospheric Entry," *Journal of Spacecraft and Rockets*, Vol. 56, No. 3, 2019, pp. 854–864. https://doi.org/10.2514/1.A34297.

[3] Woffinden, D., Robinson, S., Williams, J., and Putnam, Z. R., "Linear Covariance Analysis Techniques to Generate Navigation and Sensor Requirements for the Safe and Precise Landing Integrated Capabilities Evolution (SPLICE) Project," *AIAA Scitech 2019 Forum*, 2019. https://doi.org/10.2514/6.2019-0662.

[4] Williams, J., Woffinden, D., and Putnam, Z. R., "Mars Entry Guidance and Navigation Analysis Using Linear Covariance Techniques for the Safe and Precise Landing – Integrated Capabilities Evolution (SPLICE) Project," *AIAA Scitech 2020 Forum*, 2020. https://doi.org/10.2514/6.2020-0597.

[5] Markley, J., and Carpenter, J., "Generalized Linear Covariance Analysis," *The Journal of the Astronautical Sciences*, Vol. 57, No. 1-2, 2009, pp. 223–260. https://doi.org/10.1007/BF03321503.

[6] Luo, J., et al., "Robust Entry Guidance Using Linear Covariance-based Model Predictive Behavior," *International Journal of Advanced Robotic Systems*, Vol. 14, No. 1, 2017. https://doi.org/10.1177/1729881416687503.

[7] Braun, R. D., and Manning, R. M., "Mars Exploration Entry, Descent, and Landing Challenges," *Journal of Spacecraft and Rockets*, Vol. 44, No. 2, 2007, pp. 310–323. https://doi.org/10.2514/1.25116.

[8] Lorenz, C. G., and Putnam, Z. R., "Entry Trajectory Options for High Ballistic Coefficient Vehicles at Mars," *Journal of Spacecraft and Rockets*, Vol. 56, No. 3, 2019, pp. 811–822. https://doi.org/10.2514/1.A34262.

[9] Dutta, S., and Braun, R. D., "Statistical Entry, Descent, and Landing Performance Reconstruction of the Mars Science Laboratory," *Journal of Spacecraft and Rockets*, Vol. 51, No. 4, 2014, pp. 1048–1061. https://doi.org/10.2514/1.A32937.

[10] D'Souza, C., and D'Souza, C., *An optimal guidance law for planetary landing*, 1997. https://doi.org/10.2514/6.1997-3709, URL https://arc.aiaa.org/doi/abs/10.2514/6.1997-3709.

[11] Geller, D. K., "Linear Covariance Techniques for Orbital Rendezvous Analysis and Autonomous Onboard Mission Planning," *Journal of Guidance, Control, and Dynamics*, Vol. 29, No. 6, 2006, pp. 1404–1414. https://doi.org/10.2514/1.19447.

[12] Pierrottet, D. F., Amzajerdian, F., Petway, L. B., Hines, G. D., and Barnes, B., *Field Demonstration of a Precision Navigation Lidar System for Space Vehicles*, 2013. https://doi.org/10.2514/6.2013-4717.

[13] Pierrottet, D. F., Hines, G., Barnes, B., Amzajerdian, F., Petway, L., and Carson, J. M., *Navigation Doppler Lidar Integrated Testing Aboard Autonomous Rocket Powered Vehicles*, 2013. https://doi.org/10.2514/6.2018-0614.

[14] Zanetti, R., Woffinden, D., and Sievers, A., "Multiple Event Triggers in Linear Covariance Analysis for Spacecraft Rendezvous," *Journal of Guidance, Control, and Dynamics*, Vol. 35, No. 2, 2012, pp. 353–366. https://doi.org/10.2514/1.54965.